Fast Curve Estimation Using Pre-Conditioned Generalized Radon Transform

Kim V. Hansen
Oticon, Strandvejen 58, 2900 Hellerup,
Phone +45 39177120, e-mail kvh@Oticon.Oticon.dk400.dk.

Peter A. Toft
Department of Mathematical Modelling, Building 349,
Technical University of Denmark, 2800 Lyngby, Denmark,
Phone +45 45934207, e-mail ptoft@ei.dtu.dk

Abstract

A new algorithm for fast curve parameter estimation based on the generalized Radon transform is proposed. The algorithm works on binary images, obtained, e.g., by edge filtering or deconvolution. The fundamental idea of the suggested algorithm is the use of a pre-condition map to reduce the computational cost of the generalized Radon transform. The pre-condition map is composed of irregular regions in the parameter domain, which contain peaks that represent curves in the image. To generate the pre-condition map, a fast mapping procedure named *image point mapping* is developed. As the image point mapping scheme maps image points into the corresponding parameter values in the parameter domain, it is possible to improve computational efficiency be recognizing image points with value zero. Initially, the suggested algorithm estimates the pre-condition map and subsequently applies the generalized Radon transform within the regions specified by the pre-condition map. The required parameter domain sampling and the resulting blurring are also investigated.

The suggested algorithm is successfully applied to the identification of hyperbolas in seismic images, and two numerical examples are given.

1 Introduction

A recurring problem in computer image processing is the identification of curves with specific shapes. The transform developed by Hough [1] for detection of complex patterns in binary $\{0, 1\}$ digital images has been discussed by several authors, e.g., [2], [3] and generalized for multi-dimensional pattern detection in [4]. The Hough transform can be deduced [5] as a special case of a more general transform, known as the Radon transform [6]. The Radon transform is a mapping from an image domain to a parameter domain, where the parameters characterize the curves to be identified. The Radon transform can be generalized to handle arbitrary curves [7]. The Hough version of the generalized Radon transform detects specific values of parameters, as spatially extended curves are transformed to produce spatially compact features in the parameter domain. In this way, the generalized Radon transform converts a difficult global detection problem in the image domain into a more easily solved local peak detection problem in the parameter domain.

In recent years progress has been made to understand and increase the speed of the generalized Radon transform [8, 9, 4]. Investigations concerning both the traditional and more recent generalized Radon transform for curve identification schemes point out two problems with respect to computational cost. First, the estimation schemes are not capable of exploiting image points with zero value (zero image points), and second, estimation is computationally expensive, as it estimates unneeded information. This is a consequence of parameter estimation, in areas of the parameter domain where curve parameters are very unlikely.

The basis for curve parameter estimation as described in this paper is a binary image. The binary image can be produced in several ways, e.g., by edge filtering or deconvolution.

In this paper, a new algorithm for fast curve estimation, called the FCE-algorithm, is presented. The key idea of the FCE-algorithm is to pre-condition the parameter domain, creating irregular regions corresponding to the parameter regions of interest. Furthermore, the FCE-algorithm takes advantage of zero image values in generating the pre-condition map. Initially, the FCE-algorithm identifies regions of the parameter domain which contain peaks representing curves in the image. Subsequently, it estimates a traditional generalized Radon transform within these regions.

The identification of hyperbolas is of particular interest within seismic signal processing. Over the years the seismic industry has developed a method of recording seismic signals resulting in images in which the investigated reflections produce curves. The recording geometry of seismic data acquisition results in signals having the same geometrical mid point between source and receiver, see, e.g., [10]. The set of signals corresponding to the same mid point is called a common mid point gather (CMP-gather). A common technique in seismic data analysis for estimation of hyperbola parameters is velocity analysis, e.g., [11]. Within the presented work some features from velocity analysis are incorporated, however, the presented method has less computational cost.

Recently, the multipulse excited speech coding technique, which was originally proposed by Atal *et al* [12], has been suggested for seismic deconvolution by Cookey *et al.* [13]. Basically, the multipulse model for speech assumes the speech signal to be a result of several impulses transformed by the shape of the vocal tract filter. In seismic deconvolution, the input signal is often modeled as an all-pole impulse and the layered earth reflectivity model is considered as an impulse train, see, e.g., [14]. Thus, the multipulse technique can be used to map seismic signals in a CMP-gather into a binary image, where the image value is set to one in case of a reflection and zero otherwise. The reflections represent information concerning the geological structure of the subsurface.

The traditional generalized Radon transform is described in section 2. Creation of the preconditioning map is described in section 3, where the *image point mapping* procedure is developed. In section 4, parameter domain sampling is discussed and section 5 describes parameter domain blurring, which is a result of discretization. The FCE-algorithm is presented in section 6, and is applied to two numerical examples for detection of hyperbolas in section 7. Regarding notation, scalars are denoted by letters, and vectors by bold-faced letters.

2 The Generalized Radon Transform

Let $f(\kappa, t)$ be a continuous signal of the continuous variables κ and t and let $\boldsymbol{\xi}$ denote an η-dimensional parameter vector defined as

$$\boldsymbol{\xi} = (\xi_1, \ldots, \xi_i, \ldots, \xi_\eta) \tag{1}$$

where (κ, t) is called the image domain, $\boldsymbol{\xi}$ the parameter domain, and $f(\kappa, t)$ the image.

2.1 The Continuous Generalized Radon Transform

Let $F(\boldsymbol{\xi})$ denote the continuous generalized Radon transform of $f(\kappa, t)$, defined as

$$F(\boldsymbol{\xi}) = \int_{-\infty}^{\infty} f(\kappa, \phi(\kappa; \boldsymbol{\xi}))\; d\kappa \tag{2}$$

where $t = \phi(\kappa; \boldsymbol{\xi})$ denotes the transformation curve. The generalized Radon transform is the integration of $f(\kappa, t)$ along the transformation curve.

Other definitions of the generalized Radon transform can be found in the literature [5], [6]. Equation 2 can be interpreted as a generalization of the Slant Stacking technique used in geophysics, e.g., [7], but the new ideas presented in this paper can be modified to confirm with this literature.

2.2 The Discrete Generalized Radon Transform

Let $\boldsymbol{j}$ denote the η-dimensional discrete index parameter vector defined as

$$\boldsymbol{j} = (j_1, \ldots, j_i, \ldots, j_\eta) \tag{3}$$

The correspondence between the index vector $\boldsymbol{j}$ and the sampled version of the parameter vector $\boldsymbol{\xi}$ can be written as

$$\boldsymbol{\xi} = \boldsymbol{\xi}_{\boldsymbol{j}} = \boldsymbol{\theta}(\boldsymbol{j}), \quad \text{where} \quad \xi_i = \theta_i(j_i) \tag{4}$$

where $\theta_i(j_i)$ is a parameter sampling function.

If a uniform sampling of the parameter domain is chosen, the function θ_i can be written

$$\xi_i = \theta_i(j_i) = \xi_{i,min} + j_i\; \Delta\xi_i, \quad j_i = 0, \ldots, J_i - 1 \tag{5}$$

where $\xi_{i,min}$ denotes the lower limit and $\Delta\xi_i$ the sampling interval of ξ_i.

The parameter domain and image domain sampling are assumed to be uniform. The correspondence between the discrete image domain indices (m, n) and the continuous variables (κ, t) can be written as

$$\kappa = \kappa_m = \kappa_{min} + m\; \Delta\kappa, \;\; m = 0, 1, \ldots, M - 1 \tag{6}$$

$$t = t_n = t_{min} + n\; \Delta t, \;\; n = 0, 1, \ldots, N - 1 \tag{7}$$

where κ_{min} and t_{min} denote the lower limits and $\Delta\kappa$ and Δt the sampling interval of κ and t, respectively.

Substitution of Equation 4, 6 and 7 into the transformation curve gives

$$t = t_{min} + n\; \Delta t = \phi(\kappa_{min} + m\; \Delta\kappa; \boldsymbol{\theta}(\boldsymbol{j})) \tag{8}$$

From to Equation 8, the discrete index transformation curve $\phi_d(m; \boldsymbol{j})$ can be expressed as

$$\begin{aligned} \phi_d(m; \boldsymbol{j}) &= n \\ &= \text{round}\left(\frac{\phi(\kappa_{min} + m\; \Delta\kappa; \boldsymbol{\theta}(\boldsymbol{j})) - t_{min}}{\Delta t}\right) \end{aligned} \tag{9}$$

where round$(\cdot)$ rounds to the closest integer.

Let $d(m,n)$ denote the discretized version of the signal $f(\kappa,t)$, i.e., $d(m,n) = f(\kappa_m,t_n)$ and let $D(\boldsymbol{j})$ denote the discrete generalized Radon transform (GRT) of $d(m,n)$ defined as

$$D(\boldsymbol{j}) = \sum_{m=0}^{M-1} d(m, \phi_d(m;\boldsymbol{j})) \tag{10}$$

Notice, that the term $d\kappa$ has been omitted in the discrete generalized Radon transform as it is a constant due to the uniform sampling of κ. The use of rounding instead of, e.g., linear interpolation will normally not lead to problems. If necessary, interpolation can easily be incorporated in Equations 9 and 10.

3 Image Point Mapping

From Equation 2, the continuous generalized Radon transform $F(\boldsymbol{\xi})$ can be written as

$$F(\boldsymbol{\xi}) = \int_{-\infty}^{\infty}\int_{-\infty}^{\infty} f(\kappa,t)\,\delta(t-\phi(\kappa;\boldsymbol{\xi}))\,dt\;d\kappa \tag{11}$$

where $\delta(\cdot)$ is the Dirac delta function.

Analogously, the discrete generalized Radon transform, from Equation 10, can be written as

$$D(\boldsymbol{j}) = \sum_{m=0}^{M-1}\sum_{n=0}^{N-1} d(m,n)\,\delta(n-\phi_d(m;\boldsymbol{j})) \tag{12}$$

where $\delta(\cdot)$ denotes the Kronecker delta function.

Equation 12 shows that each image point (m,n) is transformed into a parameter curve where $\phi_d(m;\boldsymbol{j}) = n$. Thus mapping of image points with zero value is needless as they will not contribute to $D(\boldsymbol{j})$. The proposed estimation scheme for the Radon transform accounts for the fact that zero image values do not contribute, and does not include them in the summation in Equation 12. This has the potential to reduce the computational cost considerably.

Now, assume that ϕ is invertible in one of the parameters ξ_i, e.g., ξ_η. The inverse function $\phi_{\xi_\eta}^{-1}$ with respect to ξ_η can be written as

$$\xi_\eta = \phi_{\xi_\eta}^{-1}(\kappa,t;\boldsymbol{\xi}_r), \quad \boldsymbol{\xi}_r = (\xi_1,\ldots,\xi_{\eta-1}) \tag{13}$$

Furthermore, assume that the sampling function θ_η is invertible. Then

$$\begin{aligned} j_\eta &= \mathrm{round}(\theta_\eta^{-1}(\xi_\eta)) \\ &= \mathrm{round}(\theta_\eta^{-1}(\phi_{\xi_\eta}^{-1}(\kappa,t;\boldsymbol{\xi}_r)) \\ &\equiv \Omega_d(m,n;\boldsymbol{j}_r),\ \boldsymbol{j}_r = (j_1,\ldots,j_{\eta-1}) \end{aligned} \tag{14}$$

Equations 12 and 14, are the basis for an estimation scheme for the generalized Radon transform which is referred to here as *Image Point Mapping* (IPM). The key steps of IPM can be summarized as

1. Initialize $D(\boldsymbol{j}) = 0$ for all $\boldsymbol{j}$
2. For all image points $d(m,n)$ with a value different from zero do
   For all possible $\boldsymbol{j}_r$ do
   $\boldsymbol{j} = (\boldsymbol{j}_r, \Omega_d(m,n;\boldsymbol{j}_r))$
   $D(\boldsymbol{j}) := D(\boldsymbol{j}) + d(m,n)$

Notice, that IPM is a generalization of the Hough transform [1] extended to handle arbitrary transformation curves. Like the Hough transform, the objective of IPM is parameter identification.

The fundamental difference between GRT and IPM is, that GRT requires rounding in the image domain, whereas IPM rounds in the parameter domain, as schematically shown in Figure 1.

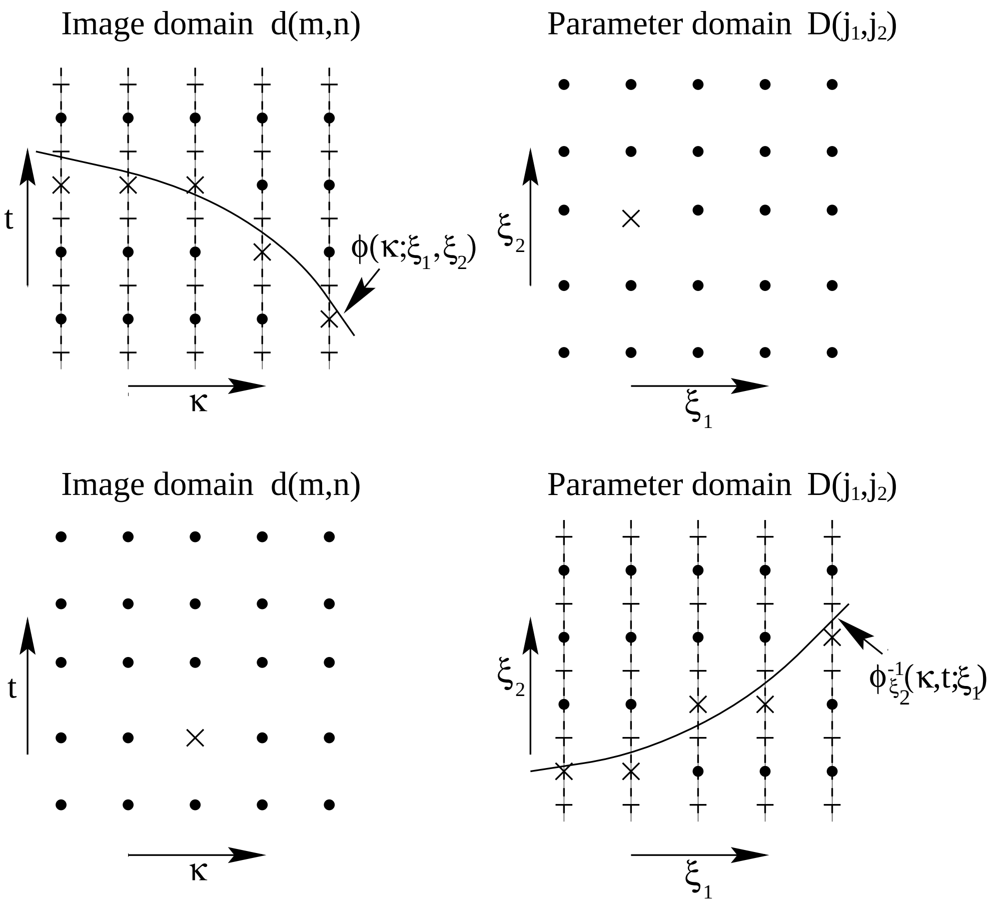

Figure 1: Top: Rounding by GRT in the image domain corresponding to a point in the parameter domain. Bottom: Rounding by IPM in the parameter domain corresponding to a point in the image domain.

The computational complexities of GRT and IPM, respectively, are

$$\begin{aligned} W_{GRT} &= O\left(M \prod_{i=1}^{\eta} J_i \right) \\ W_{IPM} &= O\left((M\,N)_r \prod_{i=1}^{\eta-1} J_i \right) \end{aligned} \tag{15}$$

where $(M\,N)_r$ indicates that only a reduced number of image points (nonzero values) are to be transformed. In Equation 15, the cost to test for nonzero values is assumed to be negligible.

The major advantage of IPM over GRT is the ability of IPM to ignore image points with a value of zero, making IPM especially well suited for sparse binary images.

If the absolute value between two successive j_η values is greater than one, i.e.,

$$|\Omega_d(m,n;\boldsymbol{j}_r+\boldsymbol{\varepsilon})-\Omega_d(m,n;\boldsymbol{j}_r)|>1 \tag{16}$$

where vector $\boldsymbol{\varepsilon}$ contains zeros at all $\eta-1$ entries and holds unit value at entry i, i.e., $\varepsilon_i=1$, it is seen that IPM will map the image point (m,n) into a perforated hypercurve, i.e., a hypercurve containing missing sections. Identification of curve parameters can be difficult due to the presence of perforation holes depending on the shape and depth of the holes.

For $\eta=2$ the perforation problem can be eliminated simply by adding $d(m,n)$ to $D(\boldsymbol{j})$ for the parameter values skipped between two successive parameter vectors. Consider, for example, the hyperbolic transformation curve as illustrated in Figure 2, where the parameter domain is described by $(j_1,j_2)=(s,z)$.

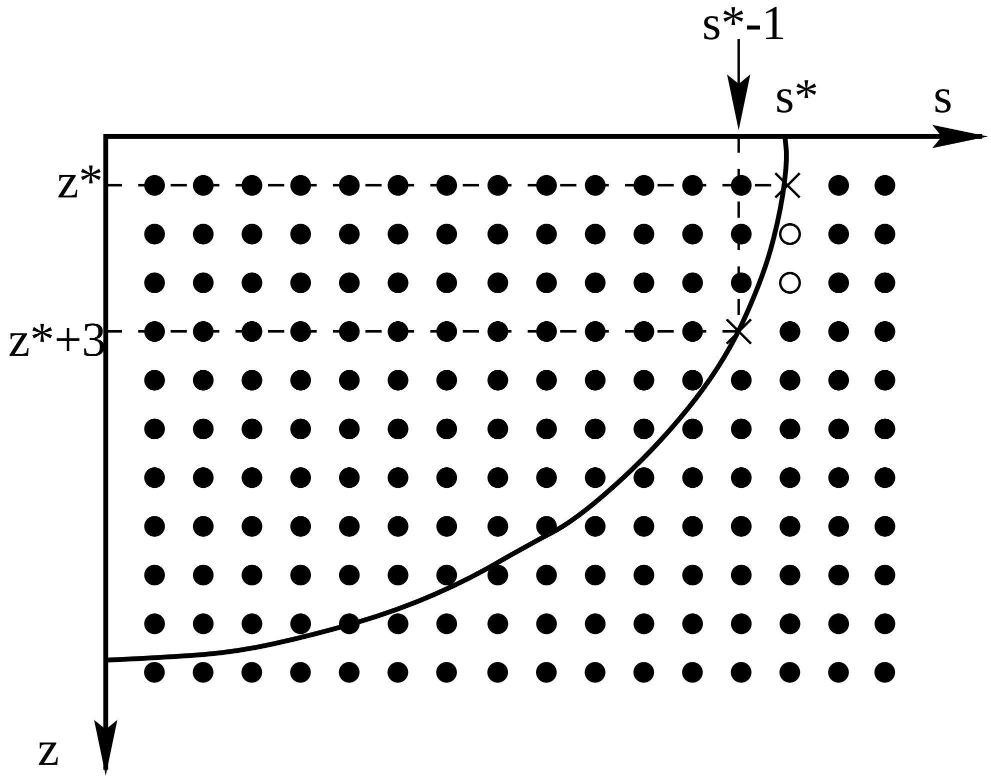

Figure 2: Illustration of the perforation problem.

Figure 2 shows the mapping of an image point (m^*,n^*) to the parameter domain, that is, discretized parameter point accumulators to which the value $d(m^*,n^*)$ of the image point must be added. To investigate the perforation problem, two parameter points (s^*-1,z^*+3) and (s^*,z^*) on the inverse transformation curve are considered. Following the inverse transformation curve from (s^*-1,z^*+3) to (s^*,z^*) along the s axis gives only the two parameter points (s^*-1,z^*+3) and (s^*,z^*). However, following the inverse transformation curve along the z axis also gives the two intervening points (s^*,z^*+2) and (s^*,z^*+1). One way of handling such intervening points is to add the value of the image point to the parameter points skipped between two successive parameter points on the inverse transformation curve. Therefore, in this example, $d(m^*,n^*)$ must be added to the skipped parameter points (s^*,z^*+2) and (s^*,z^*+1) when following the s axis.

4 Parameter Domain Sampling

For a given image $d(m,n)$ an exact determination of $\Delta\xi_i$, $\xi_{i,min}$ and J_i, which match the image, is, in general, not possible. However, some guidelines can be stated. First, some of the parameters will be bounded by the underlying physics, e.g., $\xi_{i,min}$ and $\xi_{i,max}$ will normally be limited. Second, the parameter domain can be limited by requiring that at least a fraction β of the image points addressed by the transformation curve $\phi_d(m;\boldsymbol{j})$ lie inside the image, i.e.,

$$\sum_{m=0}^{M-1} I\left\{t_{min} < \phi(\kappa_m;\boldsymbol{\xi}) < t_{max}\right\} > \beta\ M,\ \forall\boldsymbol{\xi} \tag{17}$$

where $0 < \beta < 1$, and $I\{\cdot\}$ equals 1 when the logical expression is true and 0 otherwise.

Concerning use of the GRT, the sampling intervals $\Delta\xi_i$ can be chosen by requiring that

$$\max\{|\phi(\kappa;\boldsymbol{\xi}+\boldsymbol{\gamma_i}) - \phi(\kappa;\boldsymbol{\xi})|\} \;=\; \Delta t\ \ \forall\ \kappa,\boldsymbol{\xi},\boldsymbol{\gamma_i} \tag{18}$$

where $\boldsymbol{\gamma_i}$ is a η-dimensional vector containing zeros at all entries except entry i which is $\Delta\xi_i$.

Equation 18 states that two adjacent $\boldsymbol{\xi}$-vectors give $t = \phi(\kappa;\boldsymbol{\xi})$ values which cannot be separated by more than one sample in the t-direction. This design criterion is not optimal as it leads to an unnecessarily dense sampling of certain parts of the parameter domain, however, it can be used as an upper sampling rate limit. Increasing the sampling rate of the parameter domain above a certain limit will not improve the resolution obtained by GRT as adjacent $\boldsymbol{j}$ vectors will result in the same curve $n = \phi_d(m;\boldsymbol{j})$. For GRT, a coarse sampling cannot guarantee a given curve will be detected, due to the fact that no transformation curve $\phi_d(m;\boldsymbol{j})$ can be guaranteed to follow the image curve perfectly.

Use of IPM with a dense parameter domain sampling according to Equation 18 produces curves $j_\eta = \Omega_d(m,n;\boldsymbol{j}_r)$ for (m,n) values corresponding to an image curve which do not intersect in a parameter point $\boldsymbol{j}$, but will spread out over several parameter points. The reason for this spread is the individual treatment of image points as regions of zero size and not regions of, e.g., rectangular shape. This spread can be compensated by the use of a coarse sampling of the parameter domain. In addition, a coarse sampling will lead to a lower computational cost.

Summarizing, GRT requires a dense parameter domain sampling, while IPM gives rise to blurring in the parameter domain in the case of dense parameter domain sampling, but works well with a coarse sampling of the parameter domain. This observation is the basis for the curve parameter estimation algorithm, presented in section 6.

5 Parameter Domain Blurring

Parameter domain blurring achieved by use of GRT can be interpreted in a way that makes it usable for parameter clustering. According to Equation 2 the continuous transformation curve can be written as

$$t = \phi(\kappa;\boldsymbol{\xi}), \qquad \kappa \in [\kappa_{min},\kappa_{max}] \tag{19}$$

Let Δt denote the sampling interval of t and let $\alpha\Delta t$ be a given uncertainty of t, e.g., $\alpha = 0.5$. For a parameter vector $\boldsymbol{\xi} = \boldsymbol{\theta}(\boldsymbol{j})$ to lie inside a band of width $2\alpha\Delta t$, symmetrically positioned around the image curve $t = \phi(\kappa;\boldsymbol{\xi}')$, it must satisfy the following inequality

$$t - \alpha\ \Delta t < \phi(\kappa;\boldsymbol{\xi}) < t + \alpha\ \Delta t \tag{20}$$

$$t = \phi(\kappa;\boldsymbol{\xi}'),\ \ \forall\kappa \in [\kappa_{min},\kappa_{max}] \tag{21}$$

Several parameter vectors $\boldsymbol{\xi}$ will correspond to image points within the band specified in Equation 21. Therefore, in general, a band in the image around a given curve described by the parameter vector $\boldsymbol{\xi}'$ will give rise to a region in the parameter space which consists of parameter vectors that correspond to curves inside the image band. These regions are named *clusters* and the corresponding image curve with parameter $\boldsymbol{\xi}'$ is called a *center curve*. An example of a curve band around a center curve and the corresponding parameter cluster is illustrated in Figure 3.

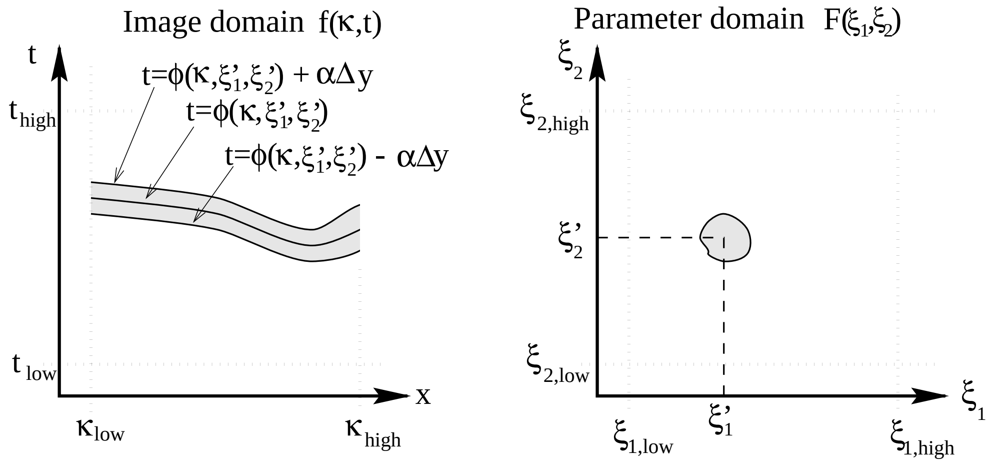

Figure 3: Left: Center curve with an uncertainty of $2\alpha\Delta t$ indicated. Right: Cluster corresponding to center curve.

Unfortunately, the center curves are normally unknown, and it is impossible to determine the clusters. However, it is possible to determine whether two parameter sets $\boldsymbol{\xi}_1$ and $\boldsymbol{\xi}_2$ belong to the same cluster. If two parameter vectors belong to the same cluster they must satisfy

$$|\phi(\kappa;\boldsymbol{\xi}_1) - \phi(\kappa;\boldsymbol{\xi}_2)| < 2\ \alpha\ \Delta t, \quad \kappa \in [\kappa_{min}, \kappa_{max}] \tag{22}$$

Parameter domain points may be gathered into regions or clusters, with the guarantee that all possible image curves will be represented by only one cluster in the parameter domain. This partitions the parameter domain into irregular regions, which reflect the information level of the image. Clustering can also be used to estimate parameter uncertainties, e.g., the maximum and minimum parameter value within the cluster can be used to give an estimate of the parameter uncertainty as, e.g., $\frac{1}{2}(\xi_{i,max} - \xi_{i,min} + \Delta\xi_i)$. Parameter domain clustering can be performed either before or after the transform, depending on the purpose.

6 The Fast Curve Estimation Algorithm

Consider an image where the image values are represented by continuous values. This image can be mapped into a binary image $d(m,n)$, e.g., by edge filtering [15], [16] or by deconvolution [17], [13]. The proposed algorithm estimates the parameters of curves in the binary image $d(m,n)$, e.g., lines or hyperbolas.

It is well-known that direct use of the GRT is computationally expensive, and gives a lot of unnecessary information concerning estimation of curve parameters. In the light of the characteristics of GRT and IPM, a fast curve parameter estimation algorithm, the *FCE-algorithm*, is proposed which simultaneously estimates all parameters of curves having a specific shape, e.g., lines or hyperbolas. The FCE-algorithm uses IPM as a pre-conditioning procedure for GRT by selecting the regions of interest in the parameter domain. IPM is suitable for a rapid determination of regions of interest, as it works well on a coarsely sampled parameter domain and is capable of ignoring image points with a value of zero. Another important circumstance is that GRT relates the uncertainty on the estimated curve parameters to the image domain sampling, while IPM relates it to the parameter domain sampling. The FCE-algorithm is shown in Figure 4, and is summarized as follows:

1. Design the discrete parameter domain, i.e., choose $\xi_{i,min}$, J_i and $\Delta\xi_i$.

2. Design a reduced parameter domain for IPM by choosing

$$J_i' = \text{ceil}\left(\frac{J_i}{2v_{\xi_i}+1}\right) \tag{23}$$

$$\xi_{i,min}' = \xi_{min} + v_{\xi_i}\Delta\xi_i \tag{24}$$

$$\Delta\xi_i{}' = (2v_{\xi_i}+1)\Delta\xi_i \tag{25}$$

   where ceil$(\cdot)$ rounds to the nearest upper integer, and v_{ξ_i} is an integer related to the resampling (see below). Then use IPM to estimate $D_{ipm}(\boldsymbol{j'})$ as

$$D_{ipm}(\boldsymbol{j'}) = \text{IPM}\{d(m,n)\} \tag{26}$$

3. Use the threshold function T to give

$$D_t(\boldsymbol{j'}) = T(D_{ipm}(\boldsymbol{j'})) \tag{27}$$

   The threshold function T is designed to remove all insignificant parameter combinations and a suitable choice might be

$$T(D_{ipm}(\boldsymbol{j'})) = \mu(D_{ipm}(\boldsymbol{j'}) - \lambda_1 M) \tag{28}$$

   where M denotes the number of image lines, λ_1 a fraction defining the significance level, and $\mu(\cdot)$ the Hamilton step function. Having an image with one curve, IPM gives a corresponding parameter domain value of M. Choosing a threshold level of $\lambda_1 M$ allows some deviation for the image curve from the integration curve, e.g., to handle holes.

4. Resample the parameter domain to obtain $D_r(\boldsymbol{j})$. The resampling process can be written as

$$D_r(\boldsymbol{j}) = D_t(\boldsymbol{j'}) \tag{29}$$

$$j_i' = \text{round}\left(\frac{j_i - v_{\xi_i}}{2v_{\xi_i}+1}\right) \tag{30}$$

   This quickly fills the entire parameter domain where the interesting regions have value one while other regions have value zero.

5. Use GRT to estimate $D(\boldsymbol{j})$ in the regions of the parameter domain where $D_r(\boldsymbol{j})$ is not equal to zero.

$$D(\boldsymbol{j}) = \text{GRT}\left\{d(m,n)\,|D_r(\boldsymbol{j}) \neq 0\right\} \tag{31}$$

6. As in step three, use the threshold function with a new significance level λ_2 to account for use of the GRT. After the thresholding, all points in the parameter domain having a value different from zero represent curve parameters.

$$\text{Estimate: } D_{ipm}(\boldsymbol{j'}) = \text{IPM}\{\text{d(m,n)}\}$$
$$\downarrow$$
$$\text{Threshold: } D_{t1}(\boldsymbol{j'}) = \text{T}_1\{D_{ipm}(\boldsymbol{j'})\}$$
$$\downarrow$$
$$\text{Resample: } D_r(\boldsymbol{j}) = D_{t1}(\boldsymbol{j'})$$
$$\downarrow$$
$$\text{Estimate: } D(\boldsymbol{j}) = \text{GRT}\{g(m,n)|D_r(\boldsymbol{j})\}$$
$$\downarrow$$
$$\text{Threshold: } D_{t2}(\boldsymbol{j}) = \text{T}_2\{D(\boldsymbol{j'})\}$$
$$\downarrow$$
$$\text{Cluster: } D_c(\boldsymbol{j}) = \text{C}\{D(\boldsymbol{j})\}$$
$$\downarrow$$
$$\text{Curve Parameters}$$

Figure 4: Flow diagram of the FCE-algorithm.

7. Finally, the identified parameters are clustered into common image curves.

The resampling process takes each parameter point corresponding to the sampling interval $\Delta\boldsymbol{\xi}'$ and extends it to several parameter points corresponding to the sampling interval $\Delta\boldsymbol{\xi}$, $\Delta\xi_i < \Delta\xi_i'$. Thus, the FCE-algorithm operates initially in a coarsely sampled parameter domain, using IPM for determination of regions of interest. Subsequently, the sampling is refined to the required level and GRT is applied within the regions of interest.

The significance levels λ_1 and λ_2 must be chosen to reflect the parameter domain values, that can be accepted as peaks corresponding to curves in the image. In general, the precise values of λ_1 and λ_2 are not critical. For the examples, suitable ranges of values for λ_1 and λ_2 are $0.1 - 0.7$ and $0.4 - 0.8$, respectively. There are two reasons for the use of a lower acceptance level in step three. First, IPM has a tendency to blur in the parameter domain, and second, only regions of the parameter domain ensured not to contain image curves must be removed. A higher significance level in step six (λ_2) is justified by the required certainty for correct curve identification.

7 The Hyperbolic Transformation Curve

Consider a seismic CMP-gather. The multipulse technique can be used to map the seismic signals in the CMP-gather into a binary image $d(m,n)$, where $d(m,n)$ is set to one if position n of trace number m contains a reflection, and to zero otherwise. If the subsurface is assumed to be horizontally layered, it can be shown [10] that the shape of the reflection curves are hyperbolas. Traditionally, the reflection curves within the CMP-gather are described by the *normal moveout* *equation* [10], which can be written as

$$\phi(\kappa;\sigma,t_0) = t = \sqrt{t_0^2 + (\sigma\ \kappa)^2},\ \kappa \in [\kappa_{min}, \kappa_{max}] \tag{32}$$

where t denotes the two way travel time with distance κ between source and receiver, t_0 the zero offset two way travel time, and finally σ denotes the slowness. The variable κ is also known as the offset.

According to Equation 32, $\phi(\kappa;\sigma,t_0)$ can easily be inverted with respect to t_0 to yield

$$t_0 = \phi_{t_0}^{-1}(\kappa, t;\sigma) = \sqrt{t^2 - (\sigma\ \kappa)^2} \tag{33}$$

Both t_0 and σ are uniformly sampled and the parameter domain sampling is chosen in agreement with Equation 18. The discretized parameter domain is denoted z and s corresponding to t_0 and σ, respectively,

$$t_0 = t_{0,low} + z\ \Delta t_0,\ z = 0,\ldots,Z-1 \tag{34}$$

$$\sigma = \sigma_{low} + s\ \Delta\sigma,\ s = 0,\ldots,S-1 \tag{35}$$

The curve perforation described in section 3 occurs in the present case of a hyperbolic transformation curve. It is, however, eliminated by adding $d(m,n)$ to $D(s,z)$ for the parameter values skipped between two successive parameter vectors.

Assume the parameter set $(\sigma_0, t_{0,0})$ corresponds to a center curve. The parameter sets (σ, t_0) corresponding to image curves within the band of width $2\alpha\Delta t$, symmetrically positioned around the image curve $t = \phi(\kappa;\sigma_0,t_{0,0})$, can according to Equation 21 be written as

$$t - \alpha\ \Delta t < \sqrt{t_0^2 + (\sigma\ \kappa)^2} < t + \alpha\ \Delta t \tag{36}$$

$$t = \sqrt{t_{0,0}^2 + (\sigma_0\ \kappa)^2}\ \forall\kappa \in [\kappa_{min}, \kappa_{max}] \tag{37}$$

Figure 5 illustrates four clusters in the parameter domain. The four clusters correspond to four center curves with an uncertainty of $10\Delta t$, i.e., $\alpha = 5$. Formulas for the cluster shape is shown in appendix A.

To illustrate the performance of the FCE-algorithm two numerical examples will be given.

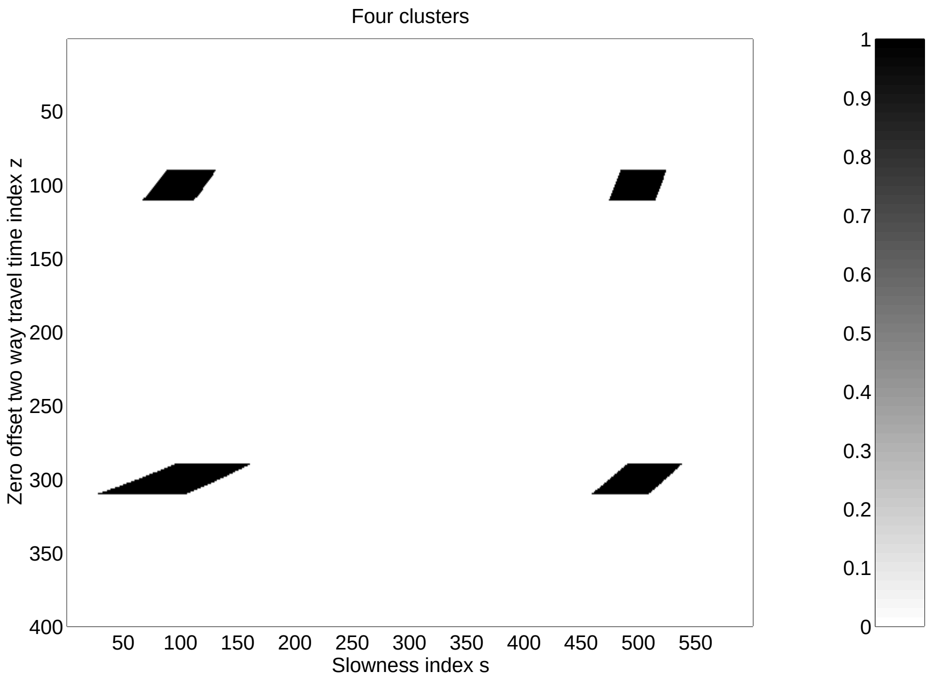

Figure 5: Four clusters in the parameter domain corresponding to an uncertainty of $10\Delta t$, i.e., $\alpha = 5$.

7.1 Example 1

In this example, the image is composed of eight hyperbolas, assembled into four groups of two hyperbolas each, as shown in Figure 6. Using GRT according to the settings in Table 1 leads to eight peaks in the parameter domain as shown in Figure 7. Thus, although the eight curves intersect and are very close, GRT is able to separate the curves in the parameter domain into eight separate peaks.

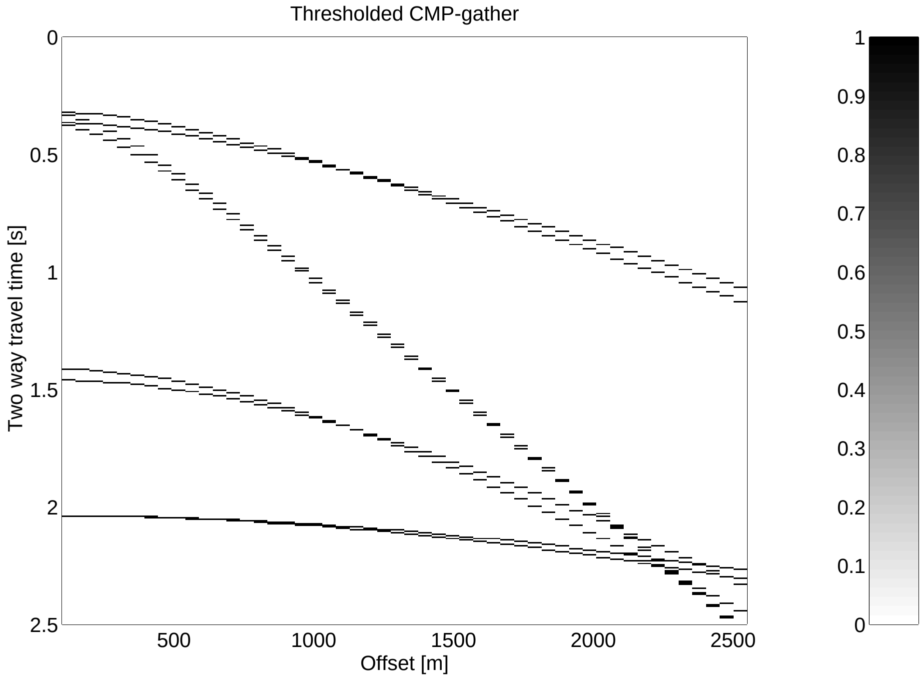

Figure 6: Synthetic binary CMP-gather composed of eight hyperbolas.

The FCE-algorithm is used for fast detection of the interesting regions in parameter domain resulting from GRT. The following five figures show each step of the FCE-algorithm. Figure 8 shows the coarsely sampled parameter domain obtained using IPM with $v_\sigma = 4$ and $v_{t_0} = 2$.

The parameter domain is thresholded using a significance level $\lambda_1 = 0.5$, and the resulting binary parameter domain is shown in Figure 9.

The binary parameter domain is then resampled to a full size parameter domain as shown in Figure 10.

Comparing this pre-condition map with Figure 7, indicates that all regions containing curves are contained within the pre-condition map. Next, Figure 11 shows the parameter domain obtained by using GRT within the regions specified by the pre-condition map.

Finally, the pre-conditioned GRT parameter domain is thresholded using a threshold level $\lambda_2 = 0.75$, and the result is shown in Figure 12.

The estimated parameter vectors are given in Table 2, where the clustering process has used a value of $\alpha = 1.5$. As seen from Table 2, eight groups of curve parameters are found, and the estimated curve parameters are rather close to the true parameters.

Image domain		Parameter domain	
Par.	Value	Par.	Value
M	50	S	300
N	400	Z	400
$\Delta\kappa$	$50\ m$	$\Delta\sigma$	$1.569 \cdot 10^{-6}\ s/m$
Δt	$4 \cdot 10^{-3} s$	Δt_0	$4 \cdot 10^{-3} s$
κ_{min}	$100\ m$	σ_{min}	$2.3 \cdot 10^{-4}\ s/m$
t_{min}	$0\ s$	$t_{0,min}$	$0 s$
α	1.5	λ_1	0.5
		λ_2	0.75
		v_σ	4
		v_{t_0}	2

Table 1: Image and parameter domain settings.

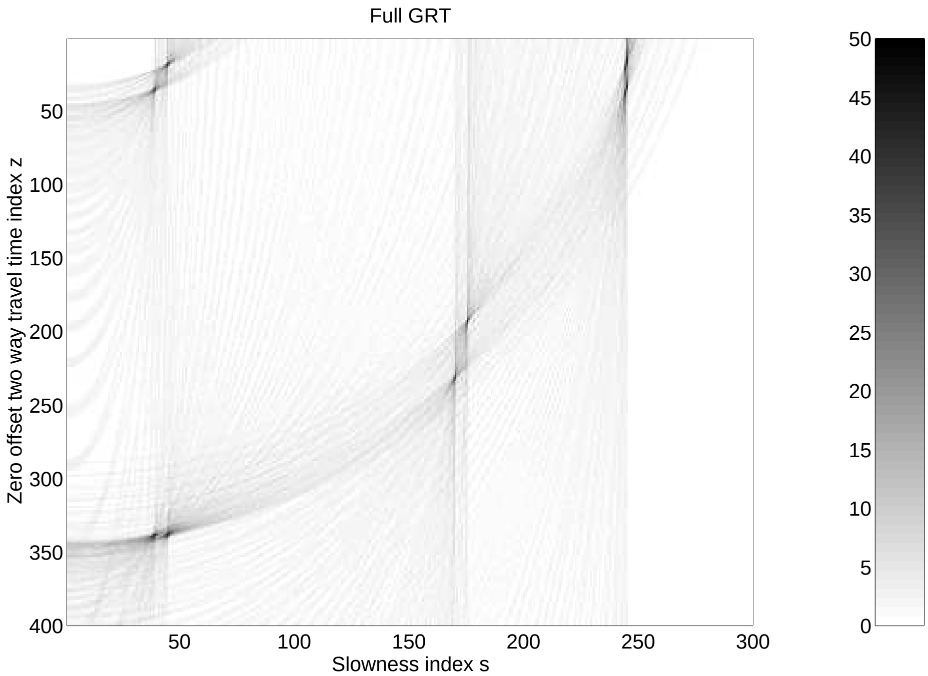

Figure 7: Full GRT estimated parameter domain.

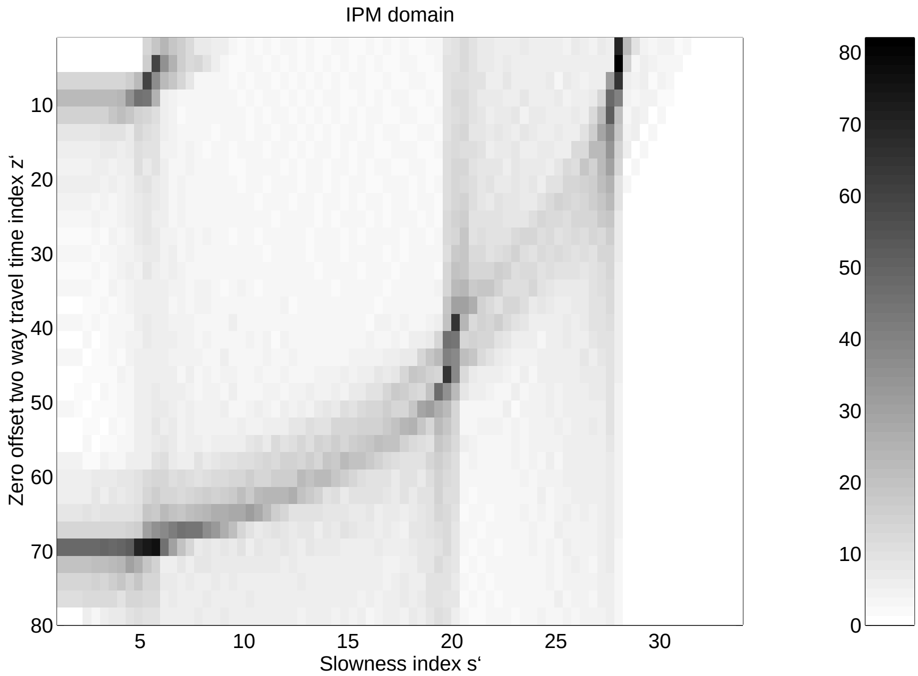

Figure 8: Parameter domain estimated by use of IPM.

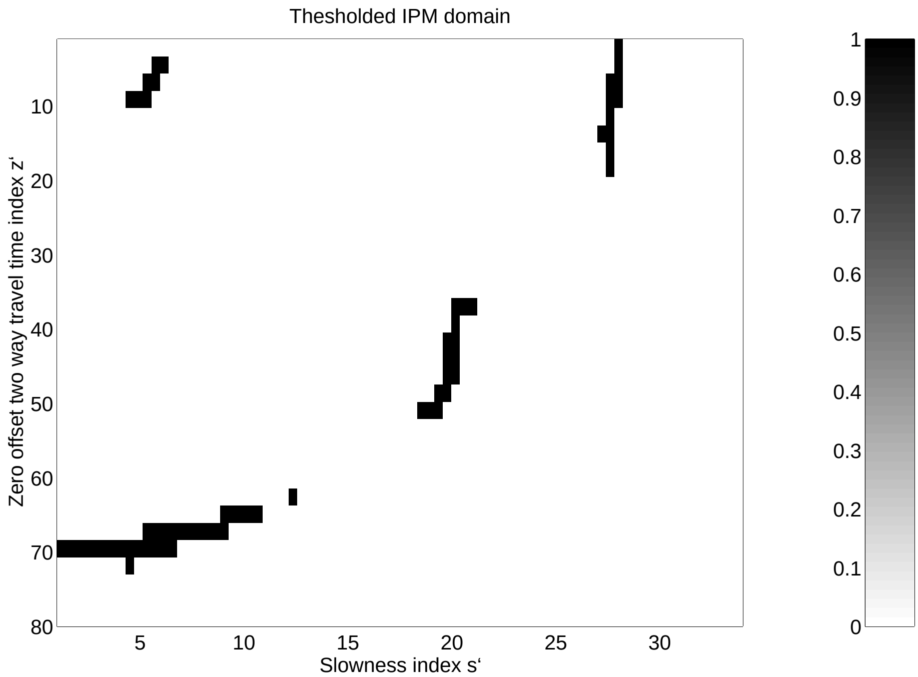

Figure 9: Thresholded IPM estimated parameter domain, where $\lambda_1 = 0.5$.

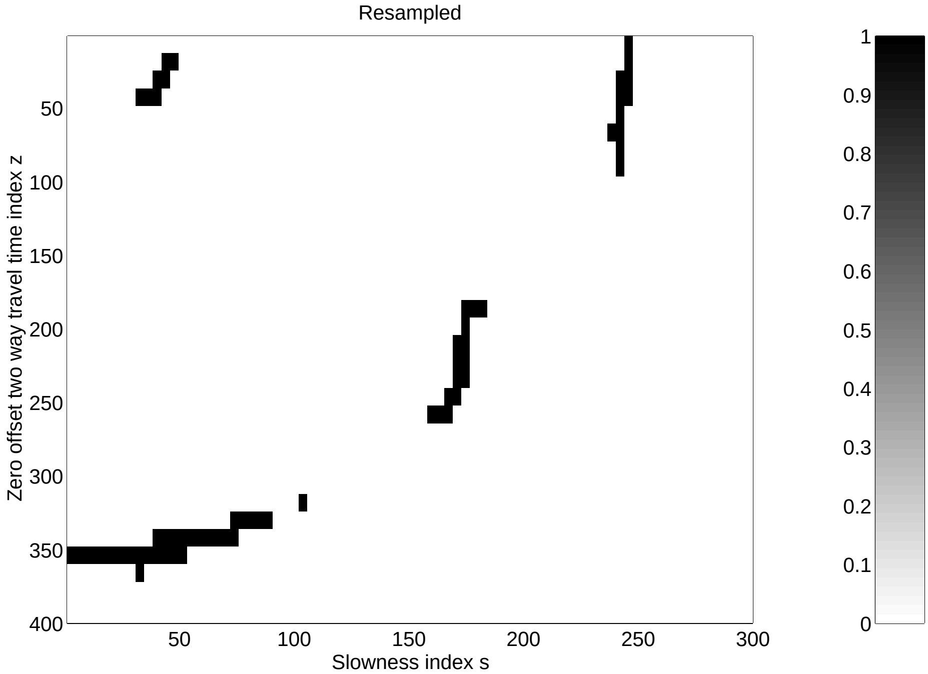

Figure 10: Resampled parameter domain.

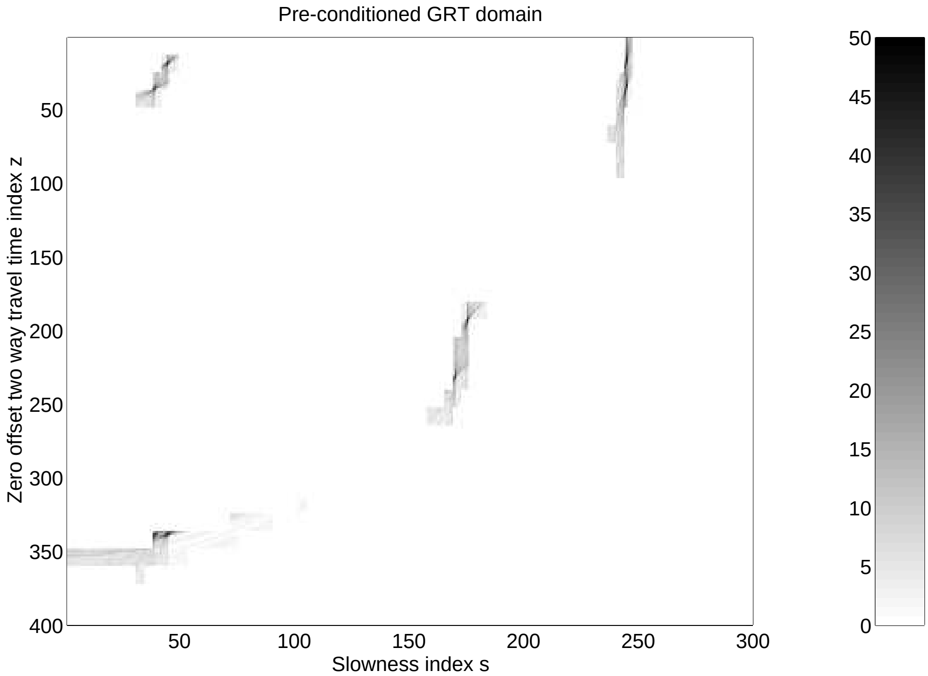

Figure 11: Parameter domain obtained using GRT within the regions specified by the resampled parameter domain shown in Figure 10.

Curve Number	Parameter
1 True	$(0.202\ s, 2.7027\ 10^{-4}\ s/m)$
1 Estimated	$(0.200\ s, 2.705\ 10^{-4}\ s/m)$
2 True	$(0.202\ s, 6.2500\ 10^{-4}\ s/m)$
2 Estimated	$(0.200\ s, 6.261\ 10^{-4}\ s/m)$
2 Estimated	$(0.204\ s, 6.245\ 10^{-4}\ s/m)$
3 True	$(0.232\ s, 2.5000\ 10^{-4}\ s/m)$
3 Estimated	$(0.232\ s, 2.503\ 10^{-4}\ s/m)$
4 True	$(0.232\ s, 6.2500\ 10^{-4}\ s/m)$
4 Estimated	$(0.232\ s, 6.245\ 10^{-4}\ s/m)$
4 Estimated	$(0.236\ s, 6.245\ 10^{-4}\ s/m)$
5 True	$(0.902\ s, 5.0000\ 10^{-4}\ s/m)$
5 Estimated	$(0.904\ s, 4.982\ 10^{-4}\ s/m)$
6 True	$(0.932\ s, 4.5455\ 10^{-4}\ s/m)$
6 Estimated	$(0.932\ s, 4.530\ 10^{-4}\ s/m)$
6 Estimated	$(0.932\ s, 4.546\ 10^{-4}\ s/m)$
7 True	$(1.302\ s, 2.7027\ 10^{-4}\ s/m)$
7 Estimated	$(1.300\ s, 2.721\ 10^{-4}\ s/m)$
7 Estimated	$(1.300\ s, 2.737\ 10^{-4}\ s/m)$
8 True	$(1.302\ s, 2.5000\ 10^{-4}\ s/m)$
8 Estimated	$(1.304\ s, 2.456\ 10^{-4}\ s/m)$
8 Estimated	$(1.304\ s, 2.472\ 10^{-4}\ s/m)$

Table 2: The results of the FCE-algorithm along with the true curve parameters. The width of the cluster band is set to 3, i.e. $\alpha = 1.5$.

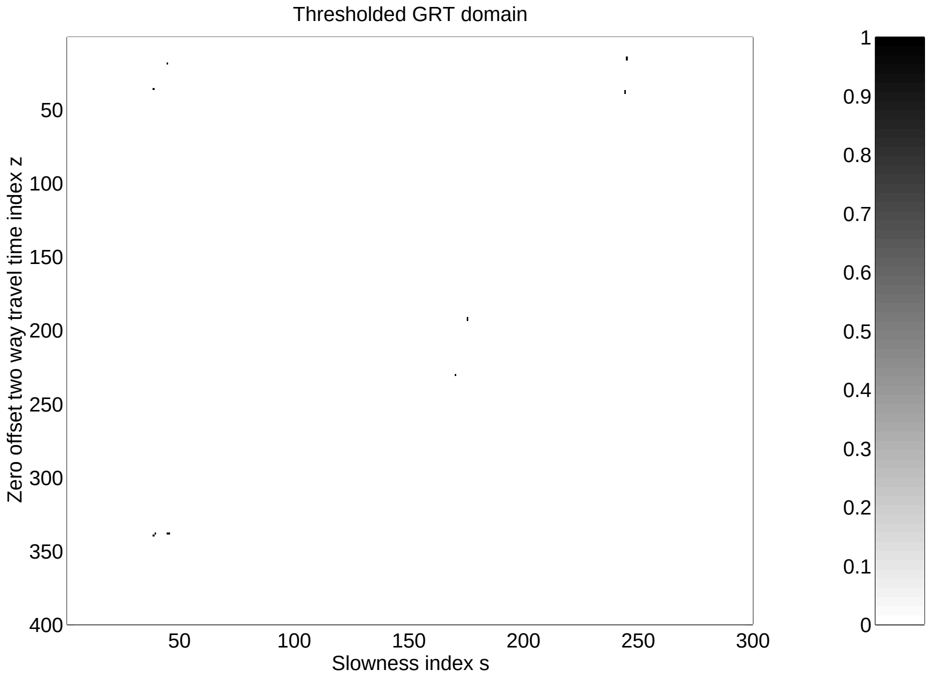

Figure 12: Thresholded GRT estimated parameter domain using $\lambda_2 = 0.75$.

7.2 Example 2

To demonstrate the performance of the FCE-algorithm in the presence of noise, an example based on a noise corrupted synthetic CMP-gather is given. The subsurface model is a pure acoustic (compressional waves only) horizontally layered subsurface consisting of four finite layers and infinite top and bottom layers. The synthetic CMP-gather is produced by use of ray tracing [10]. The resulting CMP-gather is composed of 29 reflection curves, shown in Figure 13, where each vertical line represents a trace and the signal values are illustrated using grey scale. The parameters for both image and parameter domains are given in Table 3.

In Figure 14 the corresponding true reflection curve parameters are shown, that is the values of t_0 and σ corresponding to the 29 reflection curves.

Next, the multipulse technique [12] is used to map the seismic signals in the CMP-gather into a binary image, shown in Figure 15. As seen, the mapping process results in erroneous reflections, i.e., reflections without correlation over traces. Furthermore, the reflection curves have gaps, intersect and in cases are very close. These problems are caused by the fact that the multipulse technique is a one dimensional process.

Applying the FCE-algorithm to the binary image gives the IPM estimated parameter domain shown in Figure 16, using $v_{t_0} = 2$ and $v_\sigma = 4$.

Applying GRT on the parameter domain region specified by the resampled and thresholded IPM estimated parameter domain, with $\lambda_1 = 0.5$, results in the GRT parameter domain shown in Figure 17.

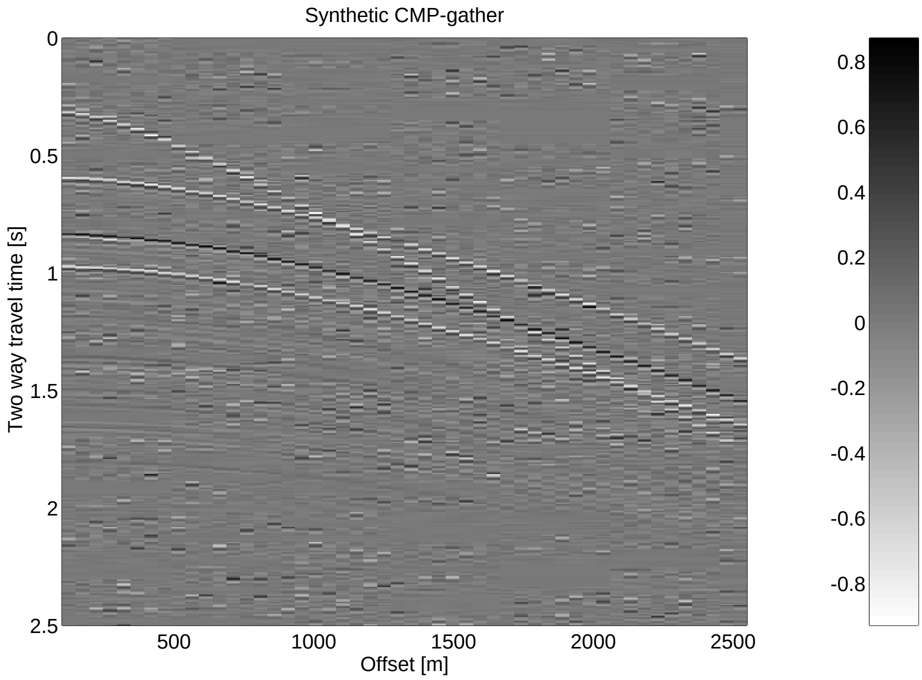

Figure 13: Synthetic CMP-gather composed of 29 reflection curves, added with uncorrelated noise.

Image domain		Parameter domain	
Par.	Value	Par.	Value
M	50	S	200
N	625	Z	625
$\Delta\kappa$	$50\ m$	$\Delta\sigma$	$1.57 \cdot 10^{-6}\ s/m$
Δt	$4 \cdot 10^{-3} s$	Δt_0	$4 \cdot 10^{-3} s$
κ_{min}	$100\ m$	σ_{min}	$4.0 \cdot 10^{-4}\ s/m$
t_{min}	$0\ s$	$t_{0,min}$	$0\ s$
α	1.5	λ_1	0.5
		λ_2	0.5
		v_σ	4
		v_{t_0}	2

Table 3: Image and parameter domain settings.

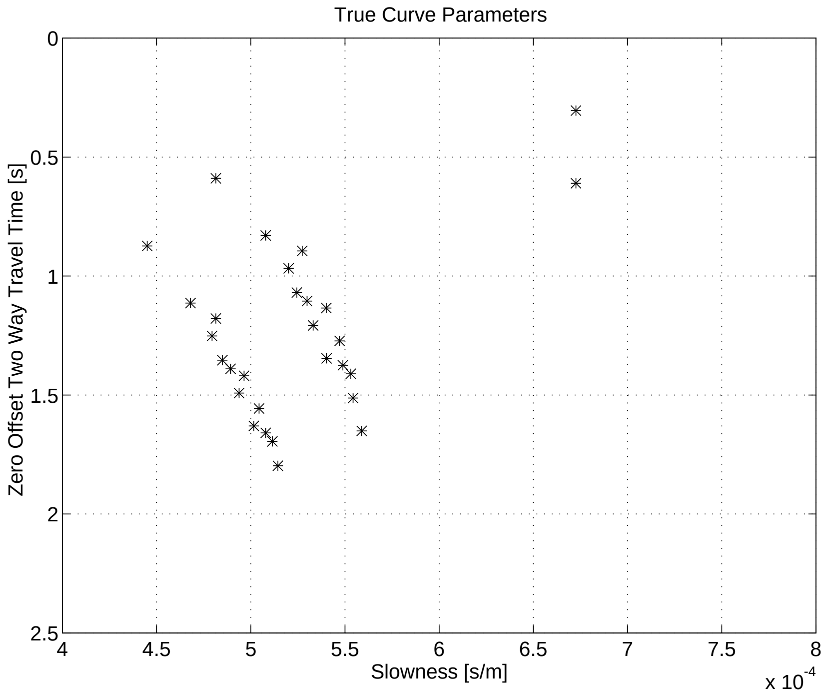

Figure 14: True reflection curve parameters.

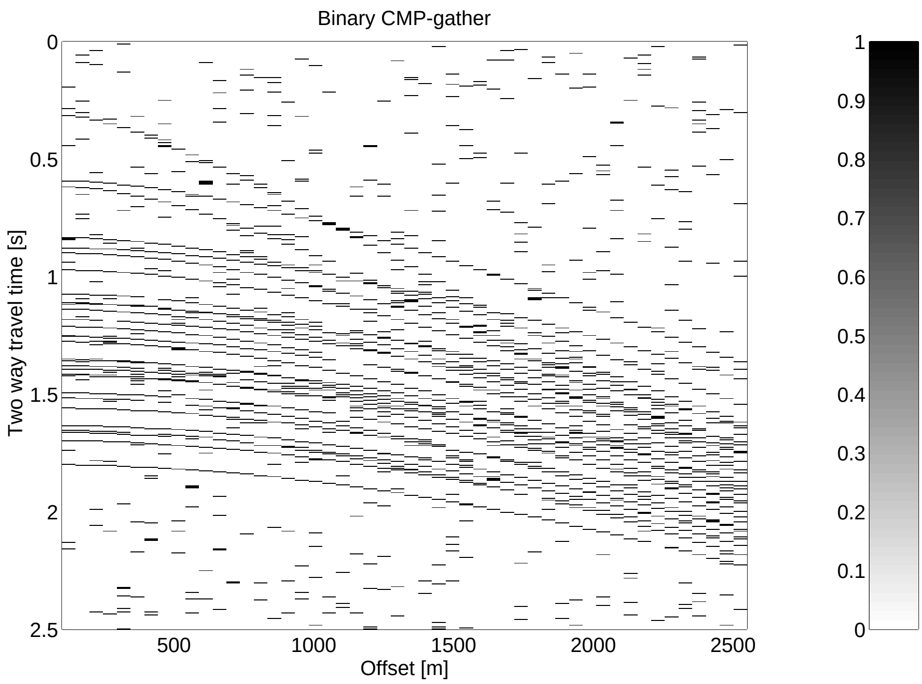

Figure 15: Binary CMP-gather obtained using multipulse technique at Figure 13.

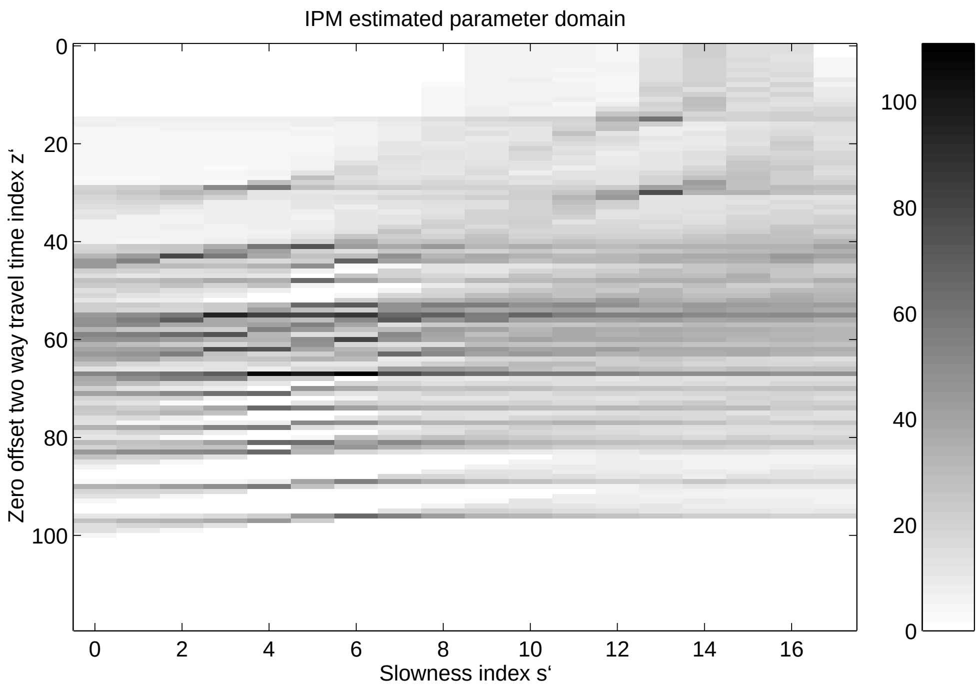

Figure 16: IPM estimated parameter domain.

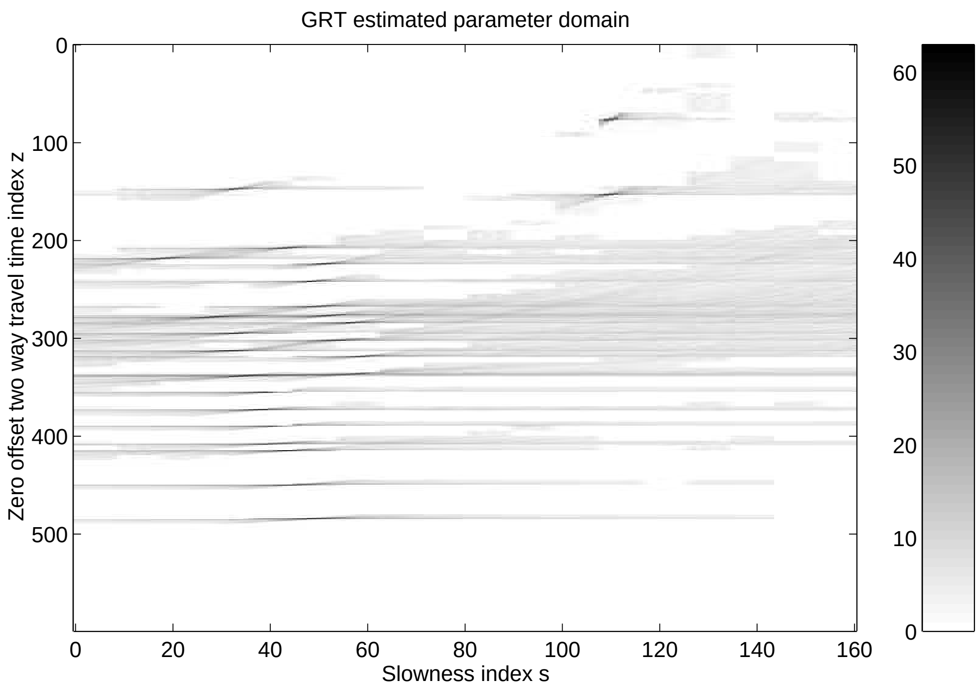

Figure 17: GRT estimated parameter domain using a pre-condition map, estimated by use of IPM.

Finally, Figure 18 shows the estimated curve parameters, where a significance level of $\lambda_2 = 0.5$ in the final threshold process and $\alpha = 1.5$ in the clustering process have been used. Comparing Figure 18 with Figure 14, which shows the true reflection curves, all reflection curves are seen to have been found, and the accuracy of the estimated reflection curves is good. The deviations of the curve parameters are less than $\pm 2 \cdot 10^{-3}$ s for t_0 and $\pm 1.5 \cdot 10^{-6}$ s/m for σ.

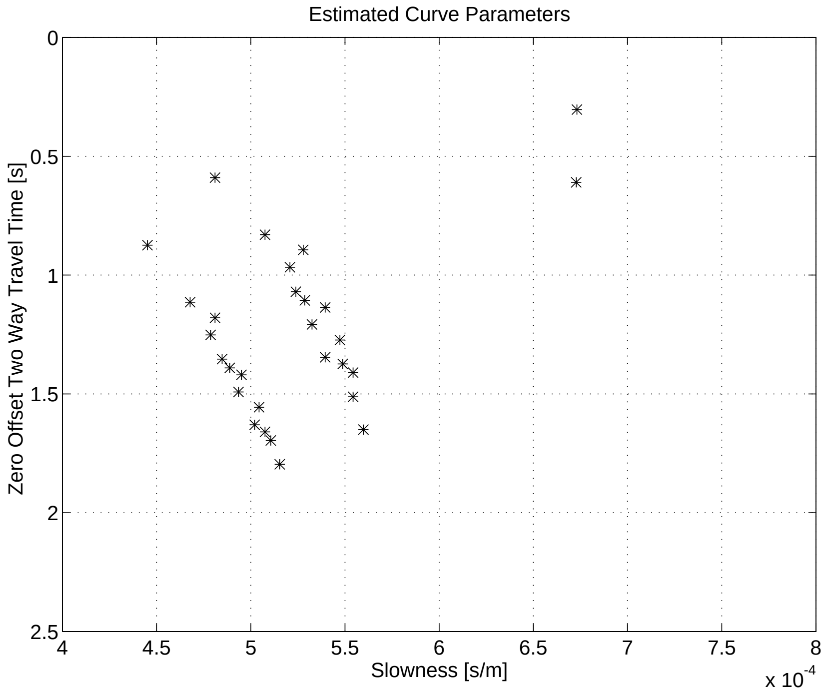

Figure 18: Estimated curve parameters using the FCE-algorithm.

8 Conclusion

A new algorithm for fast curve parameter estimation, named the FCE-algorithm, has been presented. The algorithm identifies curve parameters by operating on a binary image, obtained, e.g., by edge filtering or deconvolution.

The fundamental idea of the algorithm is the use of pre-conditioning to reduce the computational cost of the traditional generalized Radon transform. The pre-conditioning map determines regions of the parameter domain which contain peaks, and the generalized Radon transform is applied only in these regions. As the size of the regions is less than the full parameter domain, the pre-conditioning map reduces the computational costs when applying the generalized Radon transform. For fast generation of the pre-conditioning map, a generalization of the Hough transform named *image point mapping* has been developed. Image point mapping is computationally efficient by taking account of image points with value zero. The required parameter domain sampling and the resulting parameter domain blurring have been investigated.

The FCE algorithm was successfully applied to the identification of hyperbolas in seismic images and two numerical examples have been presented. One example demonstrates the potential of the algorithm for fast and accurate parameter estimation, and the other example illustrates the robustness of the algorithm with noise.

9 Acknowledgments

We wish to thank Peter Koefoed Møller, Katja Blankensteiner, Peter Skjellerup, and Jan Larsen for useful comments on this paper.

This work was partly supported by the Danish Academy of Technical Sciences and ØD-S Holding A/S.

A Clustering Using Hyperbolic Transformation Curves

In the case of hyperbolic transformation curves the exact shape of the parameter domain blurring can be calculated.

Let q denote a binary variable, $q \in \{+1, -1\}$. Thus, the lowest and highest curve within the image band specified by Equation 37 can be written

$$\sqrt{t_{0,0}^2 + (\sigma_0\ \kappa)^2} + q\ \alpha\ \Delta t = \sqrt{t_0^2 + (\sigma\ \kappa)^2} \ \Leftrightarrow$$
$$t_0^2 = \left(\sqrt{t_{0,0}^2 + (\sigma_0\ \kappa)^2} + q\ \alpha\ \Delta t\right)^2 - (\sigma\ \kappa)^2$$

It can be shown that κ_{low} and κ_{high} give the cluster limiting elliptical curves. The parameter cluster corresponding to the center curve $(t_{0,0}, \sigma_0)$ can be written as

$$\sqrt{\left(\sqrt{t_{0,0}^2 + (\sigma_0\ \kappa_{low})^2} - \alpha\ \Delta t\right)^2 - (\sigma\ \kappa_{low})^2} < t_0$$
$$< \sqrt{\left(\sqrt{t_{0,0}^2 + (\sigma_0\ \kappa_{low})^2} + \alpha\ \Delta t\right)^2 - (\sigma\ \kappa_{low})^2}$$

and

$$\sqrt{\left(\sqrt{t_{0,0}^2 + (\sigma_0\ \kappa_{high})^2} - \alpha\ \Delta t\right)^2 - (\sigma\ \kappa_{high})^2} < t_0$$
$$< \sqrt{\left(\sqrt{t_{0,0}^2 + (\sigma_0\ \kappa_{high})^2} + \alpha\ \Delta t\right)^2 - (\sigma\ \kappa_{high})^2}$$

Figure 19 (left) shows a hyperbolic center curve $(t_{0,0}, \sigma_0)$ with an uncertainty of $2\alpha\Delta t$. Figure 19 (right) shows the shape of the corresponding cluster, which is bounded by four elliptical curves. It should be noted that the cluster shape is highly dependent on the center curve $(t_{0,0}, \sigma_0)$.

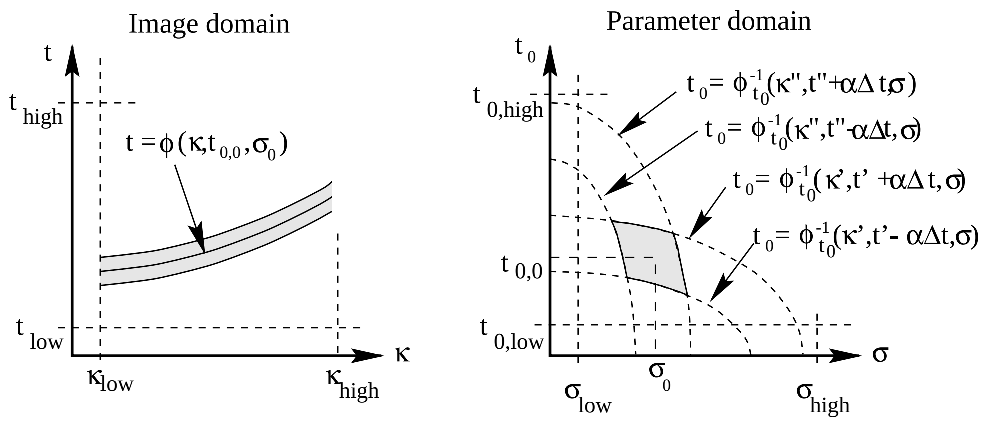

Figure 19: Left: Center curve with an uncertainty of $2\alpha\Delta t$ indicated. Right: Parameter cluster corresponding to curve band, where $\kappa' = \kappa_{low}$, $\kappa'' = \kappa_{high}$, $(t')^2 = t_{0,0}^2 + (\sigma_0\ \kappa_{low})^2$, and $(t'')^2 = t_{0,0}^2 + (\sigma_0\ \kappa_{high})^2$.

References

[1] P. V. C. Hough. A Method and Means for Recognizing Complex Patterns. US Patent: 3,069,654, Dec. 1962.

[2] R. O. Duda and P. E. Hart. Use of the Hough Transformation to Detect Lines and Curves in Pictures. *Communication of the Association for Computing Machinery*, 15(1):11–15, 1972.

[3] J. Illingworth and J. Kittler. A Survey of the Hough Transform. *Computer Vision, Graphics, and Image Processing*, 44:87–116, 1988.

[4] H. Li, M. A. Lavin and R. J. Le Master. Fast Hough Transform: A Hierachical Approach. *Computer Vision, Graphics, and Image Processing*, 36:139–161, 1986.

[5] S. R. Deans. Hough Transform From the Radon Transform. *IEEE PAMI*, 3(2):185–188, 1981.

[6] J. Radon. Über die Bestimmung von Funktionen durch ihre Integralwerte längs gewisser Mannigfaltigkeiten. *Ber. Ver. Sächs. Akad. Wiss. Leipzig, Math-Phys. Kl.*, 69:262–277, April 1917. In German. An english translation can be found in S. R. Deans: *The Radon Transform and Some of Its Applications*, app. A.

[7] S. R. Deans. *The Radon Transform and Some of Its Applications.* Krieger Publishing Company, Malabar, Florida, 2 edition, 1993. Previously John Wiley & Sons Inc., 1983.

[8] G. Beylkin. Discrete Radon Transform. *IEEE tr. ASSP*, 35(2):162–172, 1987.

[9] C. J. Haneveld and G. C. Herman. A Fast Algorithm for Computation of Radon Transforms. *Geophysical Prospecting*, 38:853–860, 1990.

[10] W. A. Schneider. The Common Depth Point Stack. *Proceesings of the IEEE*, 72(10):1238–1254, 1984.

[11] Özdoğan Yilmaz. *Seismic Data Processing.* Society of Exploration Geophysicists, Tulsa, Oklahoma, 1987.

[12] B. S. Atal and J. R. Remde. A New Model of LPC Excitation for Producing Natural-Sounding Speech at Low Bit Rates. In *Proceedings of ICASSP*, volume 1 of *ICASSP*, pages 614–617. IEEE, 1982.

[13] M. Cookey, H. J. Trussel and I. J. Won. Seismic Deconvolution by Multipulse Methods. *IEEE tr. ASSP*, 38(1):156–160, 1990.

[14] E. A. Robinson, T. S. Durrani and L. G. Peardon. *Geophysical Signal Processing.* Englewood Cliffs, New Jersey, Prentice-Hall Inc., 1980.

[15] J. Canny. A Computational Approach to Edge Detection. *IEEE tr. PAMI*, 8(6):679–698, 1986.

[16] K. Y. Huang, K. S. Fu, T. H. Sheen and S. W. Cheng. Image Processing of Seismograms: (A) Hough Transformation for the Detection of Seismic Patterns; (B) Thinning Processing in the Seismogram. *Pattern Recognition*, 18(6):429–440, 1985.

[17] C. Y. Chi, J. M. Mendel and D. Hampson. A Computationally Fast Approach to Maximum-Likelihood Deconvolution. *Geophysics*, 49(5):550–565, 1984.